

20 METER SOLAR SAIL ANALYSIS AND CORRELATION

B. K. Taleghani

NASA Langley Research Center, Army Research Laboratory, VTD, Hampton, VA

P. S. Lively

Lockheed Martin Space Operations, Hampton, VA

J. Banik

South Dakota School of Mines and Technology, Rapid City, SD

D. M. Murphy and T. A. Trautt

ATK Space Systems, Goleta, CA

ABSTRACT

This paper describes finite element analyses and correlation studies to predict deformations and vibration modes/frequencies of a 20-meter solar sail system developed by ATK Space Systems. Under the programmatic leadership of NASA Marshall Space Flight Center's In-Space Propulsion activity, the 20-meter solar sail program objectives were to verify the design, to assess structural responses of the sail system, to implement lessons learned from a previous 10-meter quadrant system analysis and test program, and to mature solar sail technology to a technology readiness level (TRL) of 5. For this 20 meter sail system, static and ground vibration tests were conducted in NASA Glenn Research Center's 100 meter diameter vacuum chamber at Plum Brook station. Prior to testing, a preliminary analysis was performed to evaluate test conditions and to determine sensor and actuator locations. After testing was completed, an analysis of each test configuration was performed. Post-test model refinements included updated properties to account for the mass of sensors, wiring, and other components used for testing. This paper describes the development of finite element models (FEM) for sail membranes and masts in each of four quadrants at both the component and system levels, as well as an optimization procedure for the static test/analyses correlation.

INTRODUCTION

Solar sails are ultra low mass (gossamer) space structures that can be used to efficiently propel spacecraft for long duration missions. Solar sails use the sun's photons^{1,2} to generate thrust without consuming fuel, which, when coupled with their light weight and favorable packaging volume, make them particularly advantageous for advanced missions.³ However, to make them effective, solar sails require enormous sail area while being as lightweight as possible. Such gossamer structures are difficult to design and analyze. These solar sails are both highly compliant and extremely nonlinear in their structural response⁴.

Adding to these difficulties is the fact that solar sail concepts proposed for space missions are impossible to fully test on the ground. While large sails could easily endure the pressure of sunlight in space, they would fail if loaded under their own weight when tested on the ground. This means that analytical models are ultimately the only method available to assess the performance of large solar sail systems before launch. To assess the accuracy of analytical models for efficiently and accurately predicting the static and dynamic behavior of large sails, smaller solar sails are analyzed and tested. Working with the smaller sail systems builds experience and confidence that the modeling techniques are adequate to accurately predict the behavior of the larger space-bound sails.

Some prior work on finite element analysis (FEA) predictions of the dynamics of solar sail systems^{4, 5} has been published, however, most sail system papers include primarily design and closed-form analysis studies⁶⁻⁸. This paper leverages previous work⁵, performed during test/analysis activities on a 10 meter solar sail system, and discusses FEA results and test/analysis correlation activities performed on the 20 meter solar sail test article.

ANALYTICAL MODEL OVERVIEW

The finite element model (FEM) for the 20 meter solar sail system was created in MSC.Patran and ran using MSC.Nastran version 2004^{9, 10}. The system model consisted of four masts and four sail quadrants with distinct properties for each sail quadrant that were based on the measured properties. In addition, the fourth quadrant included elements to represent the seams and ripstop. Figure 1 shows the overall layout of the system model.

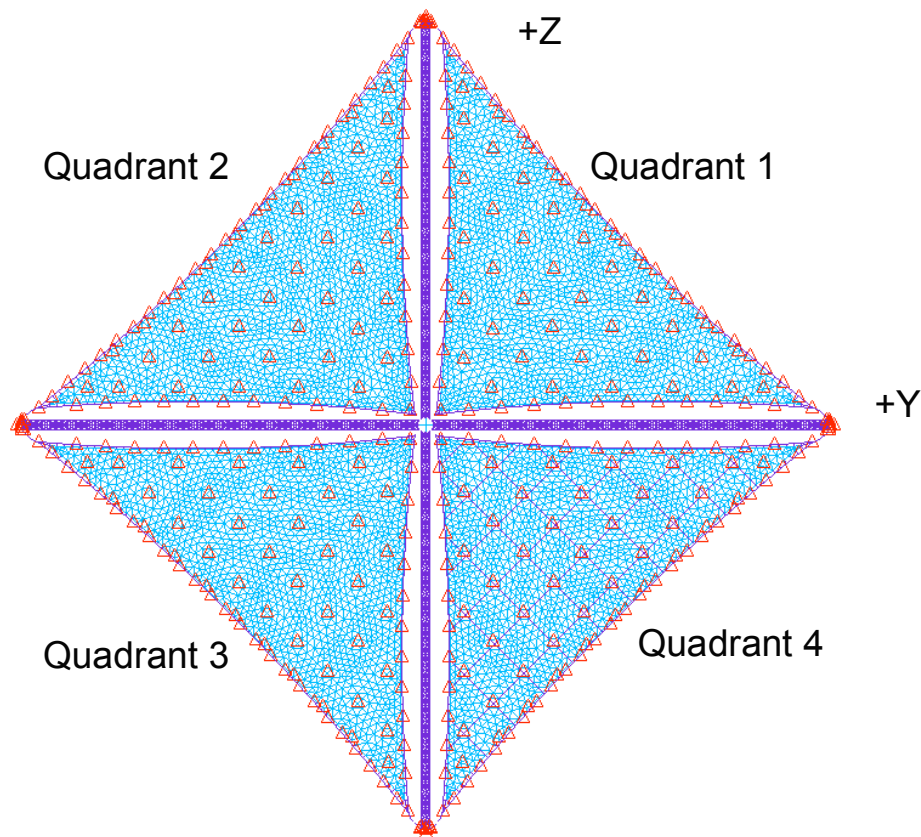


Figure 1 - 20 meter solar sail system overview

Early analyses of the complete system showed that the hub located in the center of the 20 meter system was rigid relative to the rest of the model. Consequently, the hub structure was not included in the final model of the 20 meter system. Replacing the hub structure with rigid attachments resulted in deflection changes of less than 0.003 inches and frequency shifts of less than 0.5%.

To model the four masts, beam and rod elements were used; longerons were modeled with beam elements, while the battens and the diagonals were modeled as rods since they do not

support bending. All the diagonals were modeled as tension-only elements, and they were pretensioned to 1.5 lbs. by the application of a thermal load. The layout of the mast can be seen in Figure 2.

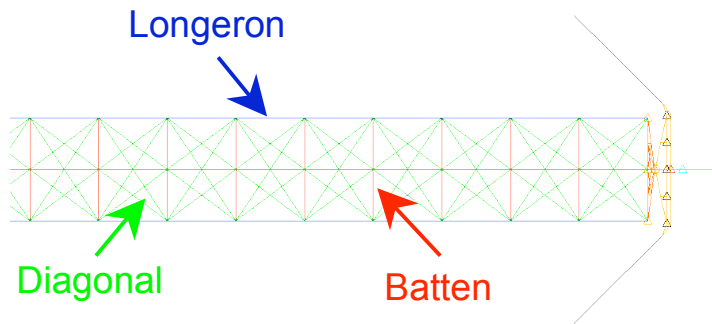


Figure 2 - Mast layout

The model of the mast tip structure was simplified from the actual test hardware but the stiffness and weight distribution were the same as the actual hardware. The mast tip consisted of two parts; a fixed part attached directly to the ends of the longerons and a rotating part allowed the spreader bars to move relative to the masts.

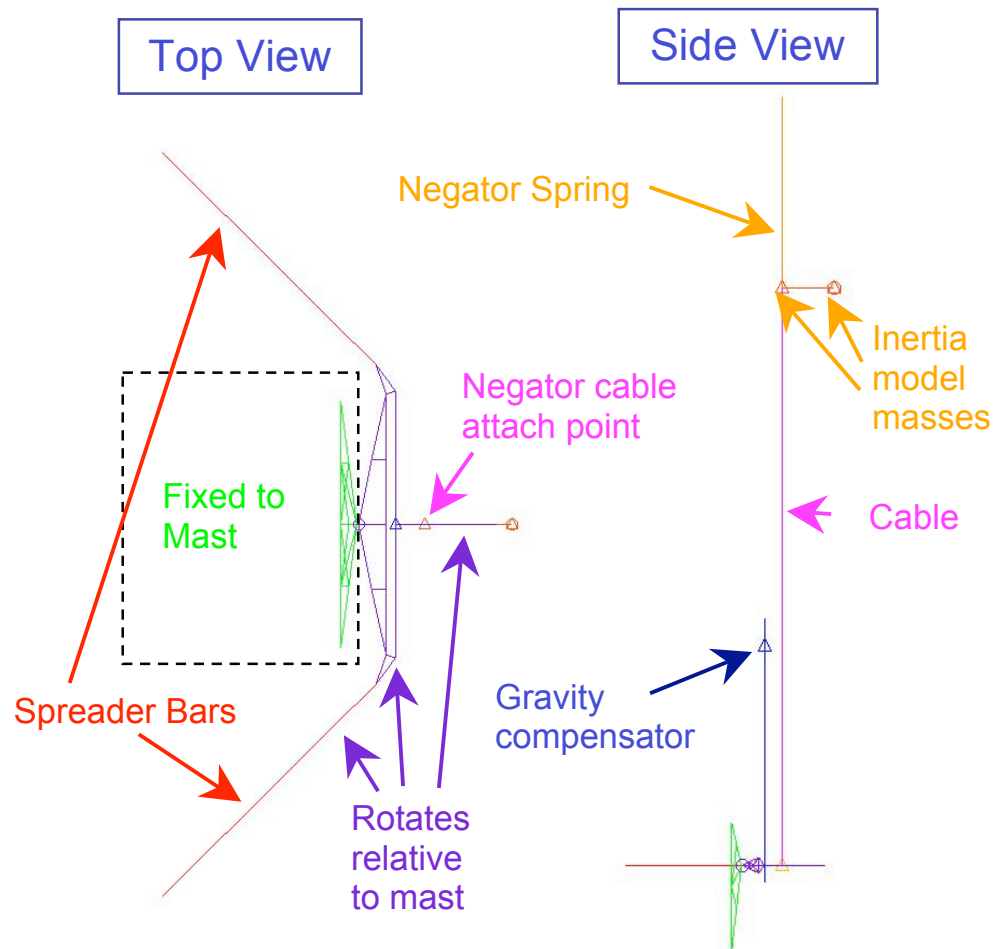


Figure 3 - Detailed views of the mast tip model

Figure 3 shows top and side views of the mast tip components that were included in the FEM. Everything outside the dashed box was included in the rotating portion of the mast tip. However the cable did not rotate with the rest of the tip structure since it was pinned to the extension bar. The cable attached to a negator spring that was pinned at the top. The negator, a constant force spring, was modeled with a very thin beam element that was pre-tensioned through thermal loading until the total force reached the desired level. Since the element was so thin, the stress-strain curve was nearly flat allowing large deflections with very little change in force. In reality the negator was a thick spool of metal tape, so masses were added to represent the rotational moment of inertia of the spool.

The gravity compensator was modeled as a mass at the end of a long beam. As the spreader bars rotated, the sail tension pulling on the spreader bars acted to bring them back to level. This produced considerable torsion loads in the masts. To counteract that load, the gravity compensator produced a countering force. As the bar tilted to the side the mass was offset from center and created torque acting in the direction of motion. The mass and the position of the mast were set to minimize the torsion loads on the masts while the spreader bars were rotated.

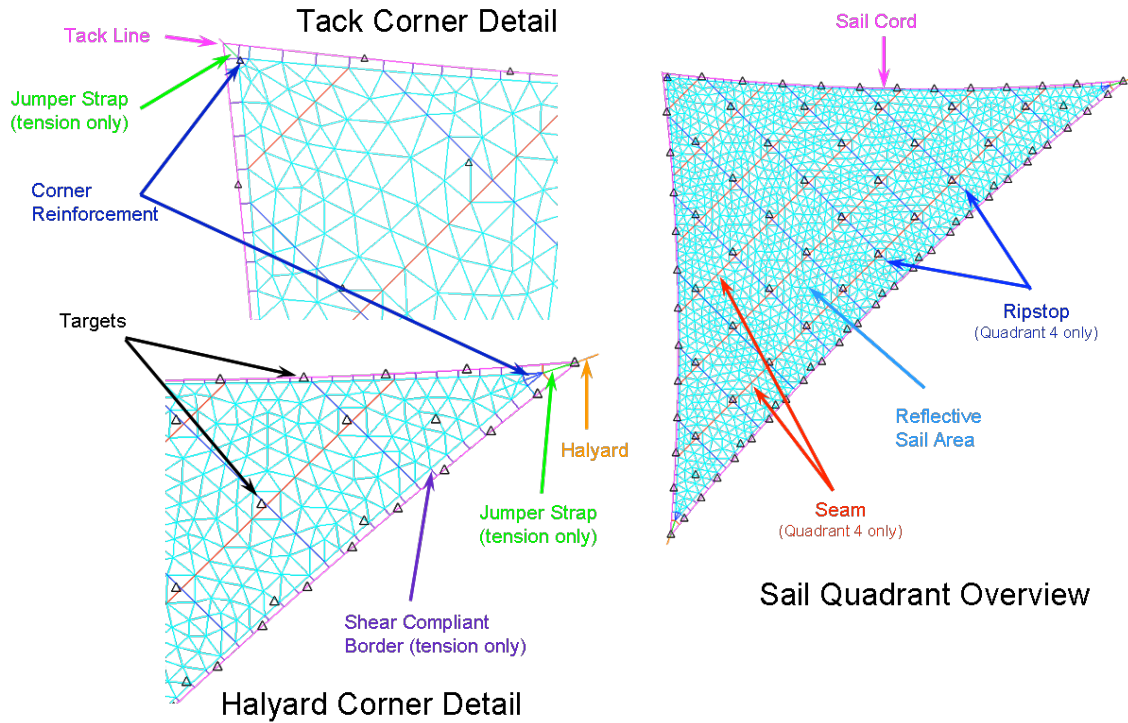


Figure 4 - 20 meter sail model view, with quadrant 4 details

The halyards from the sail attach to the masts at the tip of the spreader bars while the tack line, located at the inside corner of the sail, was pinned in place. A detailed view of the sail model can be seen in Figure 4. To model the reflective sail area, triangular TRIA3 elements and membrane properties were used with the thickness and density as shown in Table 1. Furthermore, due to irregularities in sail thicknesses a distributed mass was added to each sail quadrant to get the total weight to match the tested weight.

A shear compliant border was used to attach the reflective sail area to the perimeter cord. The shear compliant border was modeled with a series of bar elements oriented perpendicular to the edge of the reflective area. In this configuration the bar elements allowed for the transfer normal forces to the edge of the sail without transferring shear forces. The perimeter cord was modeled with beam elements.

Table 1 - Individual sail quadrant properties

| | Quadrant 1 | Quadrant 2 | Quadrant 3 | Quadrant 4 |
|-------------------------------|------------|------------|------------|------------|
| ρ (lbs/in ³) | 0.0530 | 0.0529 | 0.0529 | 0.0527 |
| t (inch) | 0.000109 | 0.000121 | 0.000127 | 0.000141 |
| Mass (lbs) | 0.8163 | 0.8883 | 0.9972 | 1.0679 |

There were a number of targets attached to the sail that were modeled as point masses. Because the locations of the targets did not align well with the mesh, and tailoring the mesh to align the targets to the nodes was not possible, these point masses were attached with multi-point constraints (MPC) to the closest nodes on the mesh. This allows the targets to be located in their real position without having to alter the mesh.

Quadrant 4 had slightly different geometry than the other three quadrants due to the inclusion of ripstop elements and seam elements. Quadrant 4 had Kevlar lines running in a grid

pattern on the sail to provide a “ripstop” mechanism. In the inboard-outboard direction (normal to the hypotenuse of the sail) the ripstop was held in place with CP1¹¹ tape. In the perpendicular direction, the ripstop was placed at the seam overlap. Ripstops and seams were modeled with beam elements and therefore the beam properties reflect both the Kevlar lines and the reinforcement material that is used to hold the ripstop in place.

The corner of the sail had a number of important details that were captured in the FEM. For example, the corner of the reflective area is reinforced with a pie-shaped piece of CP1 material on top and bottom adding 0.002 inches. Further reinforcement goes from the pie-shaped piece to the perimeter cords, effectively increasing the thickness of the shear compliant border in that area. From the corner of the pie-shape to the intersection of the perimeter cords is a jumper strap. The jumper strap is designed to be slightly slack when the sail is unloaded. As the tension in the sail is increased, the jumper strap starts taking load.

MESH STUDIES

Initial models of the solar sail were obtained using TRIA3 elements with a mesh size (average length of element edge) of 10 inches. This produced a model with enough spatial density to capture the important details while still running in a reasonable amount of time. To verify that the mesh was sufficiently dense, a mesh sensitivity study was performed.

The mesh study was conducted on only the sail portion of quadrant 4 and included the ripstop elements. The first step was to compare various densities of TRIA3 meshes to the baseline FEM. There were five meshes created with edge lengths of 5, 7.5, 10, 15, and 20 inches. For each change in edge length, a corresponding change in the number of shear compliance border elements was required. Similarly, to maintain consistency, the areas of the border elements were varied with the mesh size.

A second group of models was created based on the QUAD4 element. The QUAD4 meshes were created with 10, 20 and 30 inch element size. Smaller meshes using the quad elements were not created. A mesh with QUAD4 elements, being a higher order element type, represented the structure to the same level of accuracy as a TRIA3 mesh while utilizing fewer elements. Thus the baseline element size was used for comparison, with larger elements to see if accuracy could be maintained.

Once the meshes were created, the sails were tensioned to 6 lbs. of force in the halyard lines. After tensioning the sails, a 1-g gravity load was applied and the resulting billow shapes were compared for overall shape, maximum billow, and the centerline (from the tack line to the center of the hypotenuse) profile.

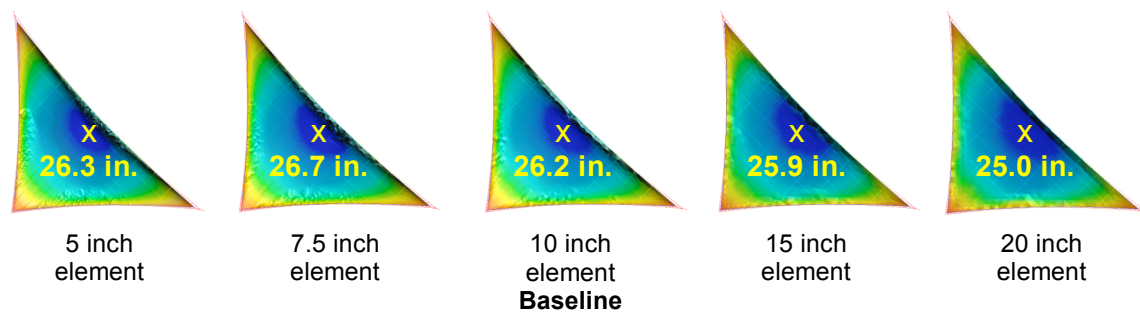


Figure 5 - Comparison of billow shape for TRIA3 models of various edge lengths

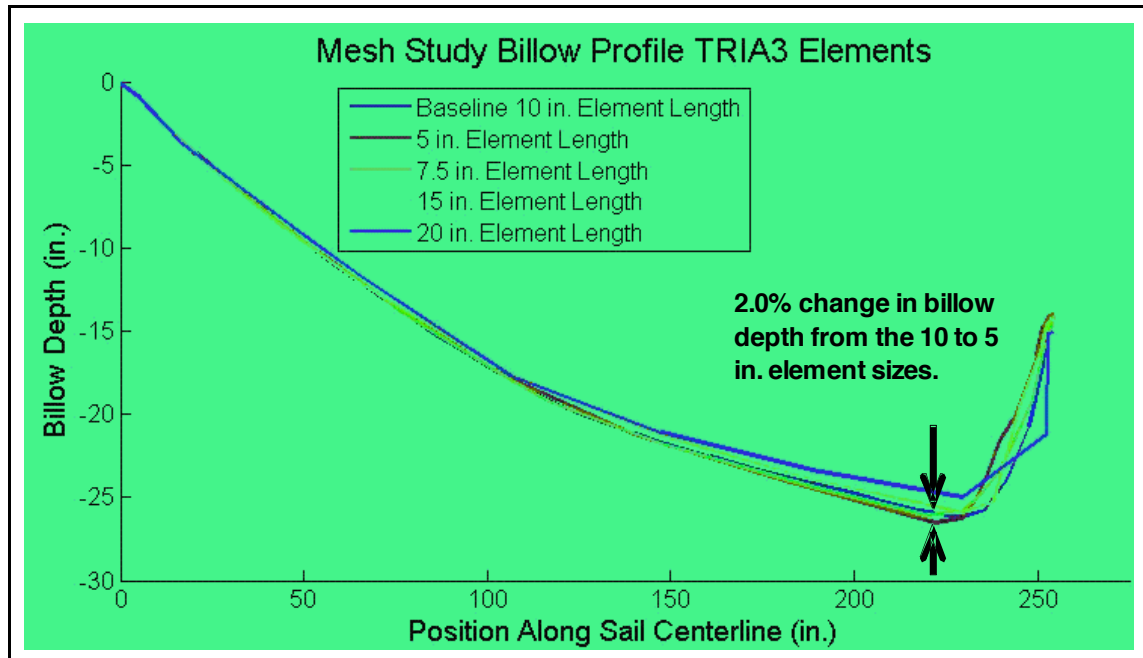


Figure 6 - Centerline billow profile for TRIA3 models of various edge lengths

Figure 5 and Figure 6 show the results of the mesh study for the TRIA3 meshes. While total billow depth is an important factor in determining consistency in the results, the actual resulting shape is more important. All of the models predict wrinkling in a z-fold wave along the perimeter of the sail; in the models with the largest element edge lengths, the wrinkles became very large and began to stiffen the structure through a corrugation effect. This is seen in the relatively low depth of the billow in the mesh with the 20 inch elements. The elements simply cannot conform to the acute curvature near the hypotenuse. It should be noted that all of the meshes show the same results toward the tack corner of the models.

Similar comparisons were performed on the QUAD4 meshes. However, the QUAD4 meshes encountered a computational issue that was not seen in the TRIA3 meshes, namely that the regularity of the mesh reinforced the z-fold pattern. This meant that the QUAD4 mesh was more likely to fold than to curve. A comparison of the wrinkling pattern for the TRIA3 and QUAD4 meshes with 10 inch elements is shown in Figure 7.

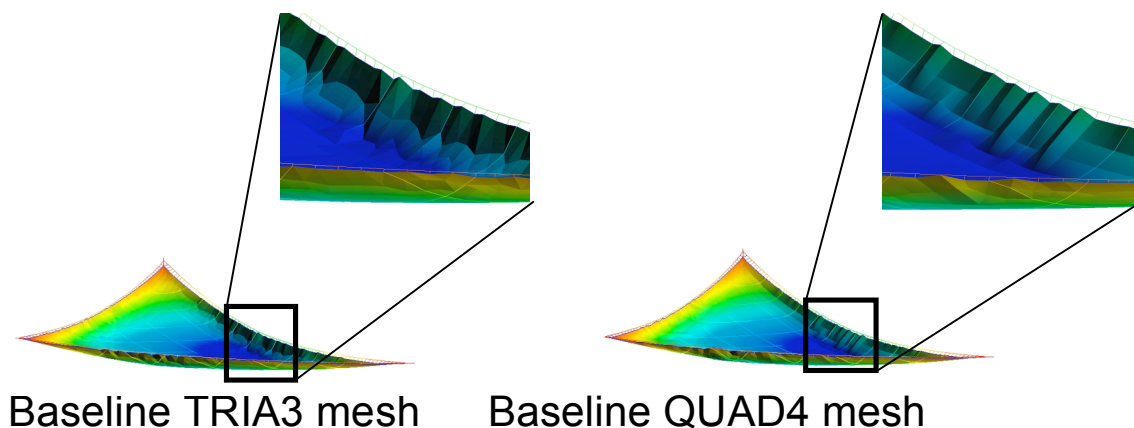


Figure 7 - Comparison of wrinkling pattern for TRIA3 and QUAD4 10-inch element meshes

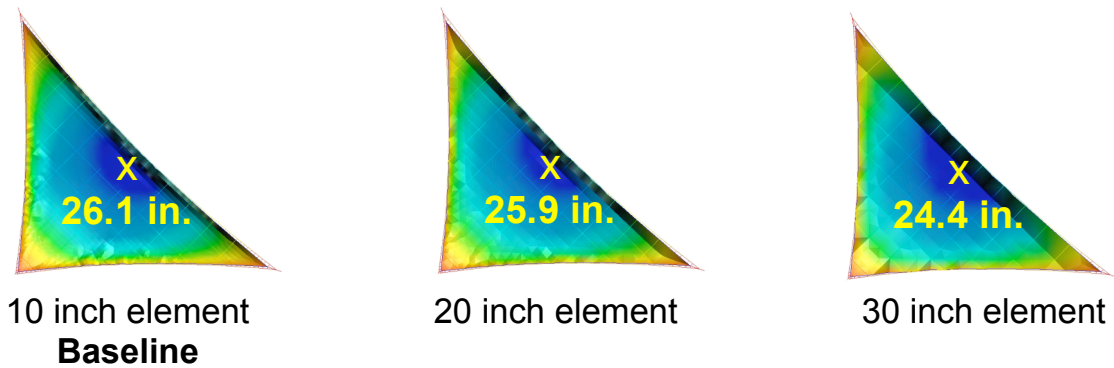


Figure 8 - Comparison of billow shape for QUAD3 models of various edge lengths

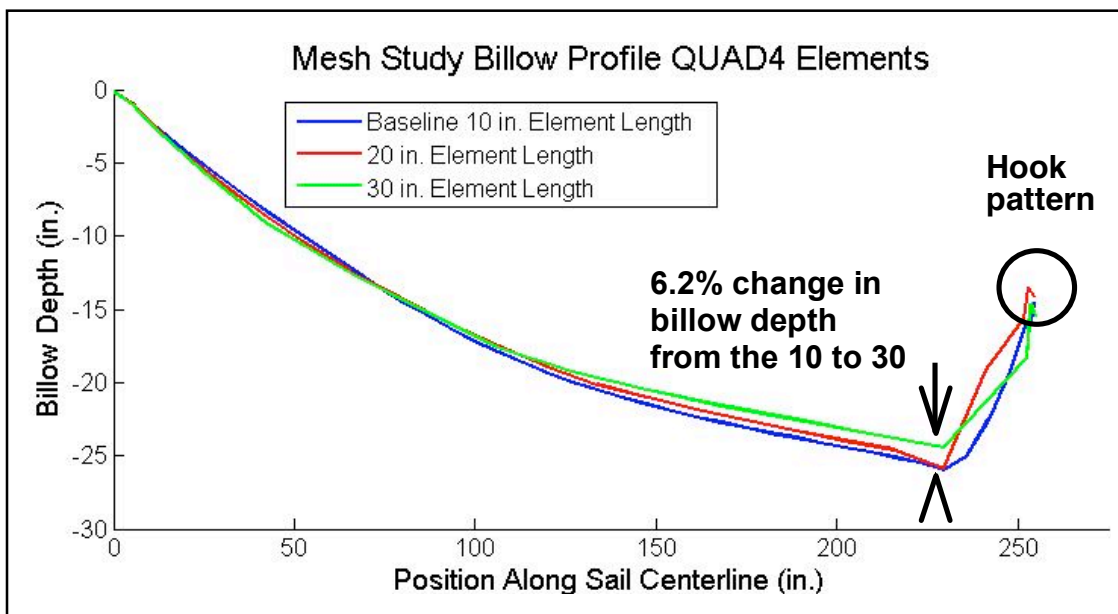


Figure 9 - Centerline billow profile for QUAD3 models of various edge lengths

Moving to a larger element size resulted in a less accurate result for the QUAD4 meshes. While the maximum billow depth is similar between the 10 inch mesh and the 20 inch mesh, as seen in Figure 8, the actual profile was considerably different. Figure 9 shows the centerline profile for the three QUAD4 meshes. For the 20 inch mesh, the model folded dramatically at the point of maximum deflection. In addition, the 20 and 30 inch meshes produced a hook pattern near the cord. This hook pattern occurred when the peak of the wrinkle pattern forced the mesh above the sail cord.

Figure 10 compares the centerline profiles of the QUAD4 mesh and the TRIA3 mesh with 10 inch element sizes. Overall, the agreement in shape is good with the QUAD4 showing slightly less overall deflection. However, the QUAD4 mesh takes over 3.5 times longer to run than the TRIA3 (1800 vs. 501 seconds) mesh, as seen in Figure 11, with less than 70% of the total number of elements.

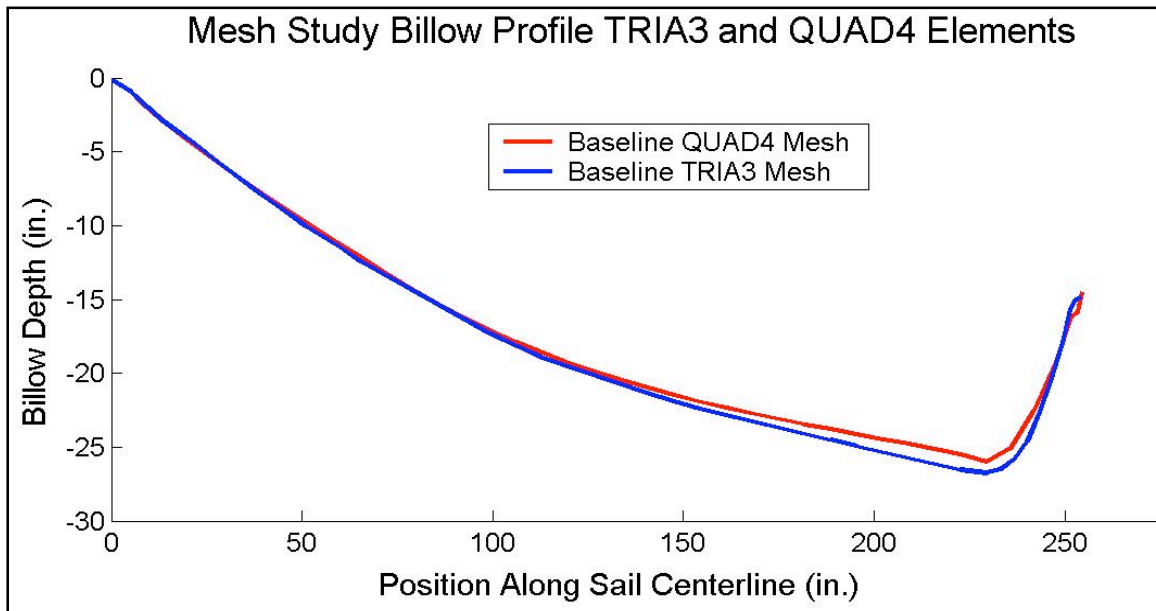


Figure 10 - Comparison of 10 inch mesh size results for QUAD4 and TRIA3 element types

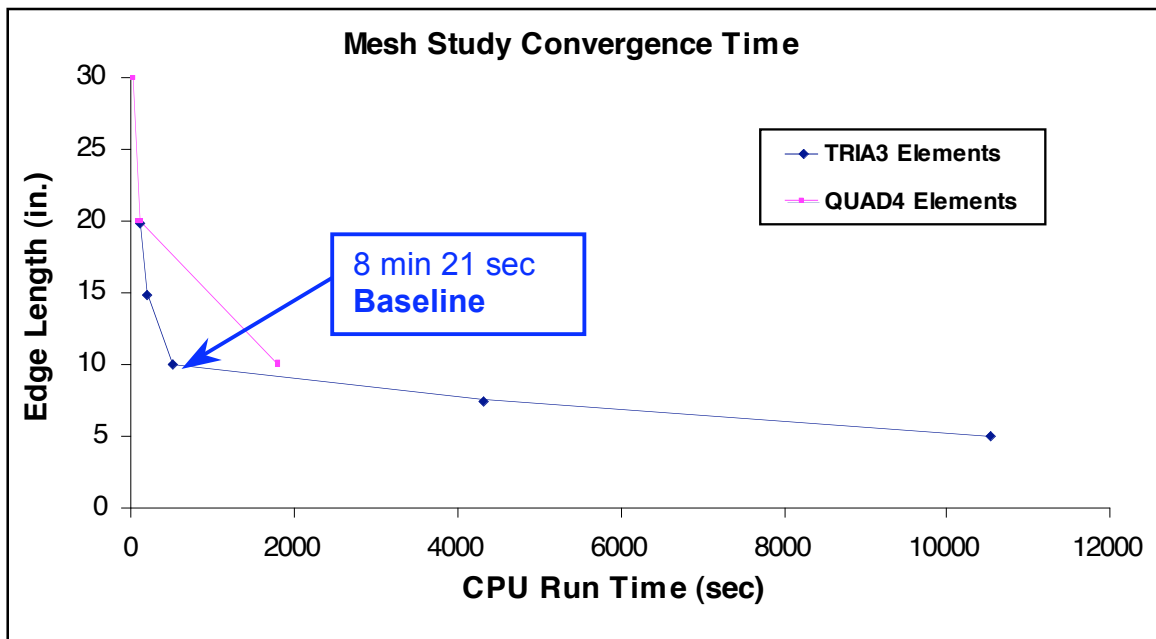


Figure 11 - Run time comparisons for TRIA3 and QUAD4 meshes of varying element lengths

Execution time increased exponentially with mesh density, as shown in Figure 11, but solution accuracy improvements were minimal. The baseline model with 10 inch elements had an acceptable run-time of around 8 minutes while showing little, if any, deterioration in the solution's accuracy.

STATIC SHAPE CORRELATION AND OPTIMIZATION

During static testing of the 20 meter solar sail system, the shape of the sail was measured using photogrammetry (PG). Targets were recorded at 44 positions for each sail quadrant in addition to locations on the mast tips and the hub structure; however, the correlation effort concentrated on the deflection shape of quadrant 4. To simplify the correlation with the test data, a FEM of quadrant 4 without the masts, mast-tips and other sails was created. Because the sail was supported at three points, it was statically determinant and could be excised from the system without any loss in accuracy. Once the quadrant 4 sail-only model was created, it was analyzed using MSC.Nastran. The billow shape was compared to the PG results. The model using nominal parameters produced a billow depth of 26.18 inches, which is nearly 30% larger than the measured billow depth of 21.87 inches. This prompted a parametric optimization effort to reduce the error in deflection shape.

OPTIMIZATION APPROACH FOR SHAPE CORRELATION

There were three steps used to change the predicted solar sail displacements to conform to the PG measured shape. The first step was the identification of parameters suspected to be in error; the second step was the creation of a response surface model; and the third step was to use the response surface model and optimization to compute a solution that minimized the error between the predictions and test.

IDENTIFICATION OF PARAMETERS

The first step in the optimization process was to identify the key parameters in the model that influenced the static deformed shape. There were two primary criteria used to select parameters. First, parameters were selected that had the greatest effect on the final results. Second, parameters must have a range of variation that would have an effect on the results, thus parameters with high certainty of their values would not be included.

Parametric studies on the 10 meter solar sail showed that the modulus of the sail material, the bending stiffness of the sail material, and the modulus and stiffness of the edge cords had little effect on the final deflection shape. Conversely, it was found that the angles of the halyards and their tensions had significant effects. In addition to the halyard angles and halyard loads, it was found that the amount of slack in the jumper straps had a profound effect on the displacement. A total of ten parameters were used in the static shape deformation optimization for the 20 meter solar sail system: 2 halyard tensions, 3 jumper strap lengths, the 3 z-offsets for the corners, and 2 halyard angles (which were varied by moving the halyards perpendicular to their lengths in the sail plane). Each parameter was assigned an expected range of variation based on either measured values (halyard loads were found to vary between 5 and 7 lbs.) or estimates based on observations (such as the distance the masts moved or the amount of slack in the jumper straps).

After the optimization effort began, it was found that the jumper strap at the tack line corner of the sail had been severed; most likely before the shape testing had been conducted. Since the parameter for the tack line jumper strap was allowed to vary enough to fully unload the strap, the optimizer could potentially identify the severed strap.

CREATION OF RESPONSE SURFACES

Even with reduced order NASTRAN models, run times prohibited traditional parameter optimization approaches. Instead, an optimization was conducted using response surface models that were created using a moving least squares method.¹² Response surface models provided a convenient way to parameterize a limited number of NASTRAN runs into a model that

could be used for optimization. A response surface is an n-dimensional interpolation function that uses previously calculated results to predict the response at another location.

To generate a response surface, the first step is to create a basis set of results. The basis consists of a set of inputs into the system (in this case the parameter values) and the outputs from the analysis (displacements of the target locations). To generate the basis, a random value was assigned to each of the ten parameters and used to generate a model. The model was analyzed and the resulting displacements for each of the targets were recorded. Hundreds of random models were created and analyzed with the parameters and the target locations recorded for each run.

The response surface is used to find an estimate \hat{y} for a desired set of parameters \vec{x} , based on existing response values $Y = \{y_1, y_2, \dots, y_N\}$ and parameters $X = \{\vec{x}_1, \vec{x}_2, \dots, \vec{x}_N\}$.

$$\hat{y}(x) = p^T \{x\} a_m(X)$$

where $p^T \{x\}$ is a polynomial basis function of order m , and $a_m(X)$ is a coefficients vector with values based on X and Y . In this analysis a quadratic basis function was used with ten parameters that gives:

$$p^T \{x\} = [1, x_1, x_2, \dots, x_{10}, x_1^2, x_1 x_2, \dots, x_{10}^2] \text{ with } m=72$$

The coefficients of $a_m(X)$ are found in a manner similar to a weighted least squares method.

$$P = \begin{Bmatrix} p^T(X_1) \\ p^T(X_2) \\ \dots \\ p^T(X_N) \end{Bmatrix}_{N \times m}$$

$$W = \begin{bmatrix} w_1(X) & \dots & 0 \\ \dots & & \dots \\ 0 & \dots & w_N(X) \end{bmatrix}_{N \times N}$$

$$A(X) = P^T W P = \sum_{i=1}^N w_i(X) p(X_i) p^T(X_i)$$

$$B(X) = P^T W = [w_1(X) p(X_1) \quad w_2(X) p(X_2) \quad \dots \quad w_N(X) p(X_N)]$$

$$a_m(X) = A^{-1}(X) B(X) Y$$

This leaves:

$$\hat{y} = p^T(x) A^{-1}(X) B(X) Y$$

The weighting function is a function of the distance from the parameter set in the basis to any other arbitrary parameter set. For a quadratic basis function:

$$w_i(x) = \begin{cases} 1 - 10\rho_i^3 + 15\rho_i^4 - 6\rho_i^5 & 0 \leq \rho_i \leq 1 \\ 0 & \rho_i > 1 \end{cases}$$

$$\rho_i = \frac{|X_i - x|}{l_i}$$

where ρ_i is the normalized distance between the point x and the domain X_i . The normalization distance l_i is selected to ensure that enough neighboring points were included to make the A matrix non-singular.

PARAMETER OPTIMIZATION

To optimize the solar sail parameters, a separate response surface was created for each of the forty-four targets on quadrant 4. The displacement estimate for each target location is compared to the actual target displacement measured during testing. The cost function for the optimization is the root-mean-square error for all of the points plus one twentieth of the maximum error. The cost function was designed to drive down the average error while not allowing significant errors at any point.

To begin the optimization, a random parameter set was chosen and the displacements for the targets estimated. A number of random parameter sets in the vicinity of the original set were estimated to determine if a better set of parameters could be found. As a new minimum was identified, the search was centered at the new point and the search radius reduced. The parameters were allowed to vary up to 25% more than the estimated parametric range. After a few iterations a new local minimum for the cost function was identified.

Once the local minimum had been identified a model was created based on those parameters. The resulting model was analyzed and the results were added to the original basis to improve the response surface predictions. This process was repeated more than a hundred times. The solution with the lowest cost function is then returned as the final solution.

As a check, the estimated solution and the actual solution were compared after every analysis. The RMS error between the estimate and the measured displacement was less than an eighth of an inch, with most of the error occurring along the hypotenuse due to wrinkling.

STATIC OPTIMIZATION RESULTS AND CORRELATION

After the optimization was performed, the resulting deflections correlated with the test results for two cases; 0° and 22° spreader bar angles. Table 2 shows the results of the optimization, with a maximum error under one inch and an RMS error of only 0.58 inches. The billow depth was defined as the z-deflection of the lowest target, whereas the P-P depth or peak-to-peak depth was the distance from the highest target to the lowest target. The maximum error was defined as the maximum vertical distance between test and analysis.

Table 2 - Optimization Results for 0 and 22.5 degree spreader bar angles

| | Test | Analysis | % error |
|--------------|-------|----------|---------|
| Billow Depth | 21.87 | 22.8 | 4.3% |
| Max. Error | | 0.96 | 4.4% |
| RMS Error | | 0.58 | 2.7% |

0 Degree Spreader Bar Angle

| | Test | Analysis | % error |
|------------|-------|----------|---------|
| P-P Depth | 25.77 | 26.3 | 2.1% |
| Max. Error | | 1.40 | 5.4% |
| RMS Error | | 0.77 | 3.0% |

22.5 Degree Spreader Bar Angle

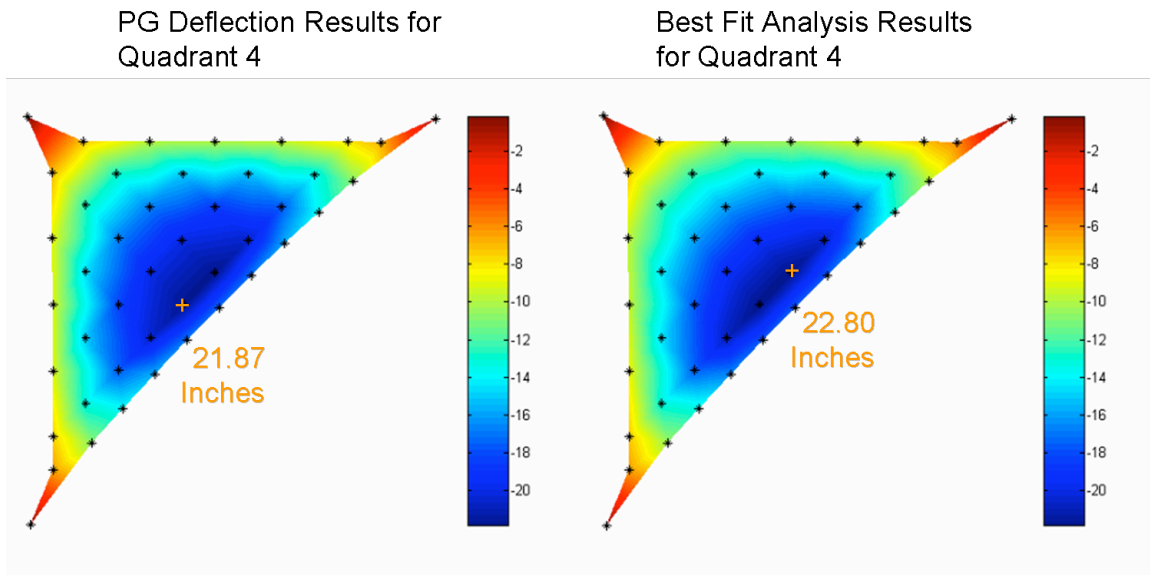


Figure 12 - Billow shape of quadrant 4 at 0 degrees for Photogrammetry (PG) and Best Fit Analysis

Figure 12 shows a side-by-side comparison of the billow profile for the test results and the analysis results. The cross indicates the point of maximum billow, which occurs at different points for the two cases. However, the two points in the analysis only vary by a tenth of an inch with a similar difference in the test results.

The resulting parameters from the optimization are shown in Table 3. The parameters were allowed to vary outside the range by 25%, so while many parameters exceeded the estimated range, none of the parameters were found to lie on the parameter limits. Also, the amount of slack in the tack line jumper strap was sufficient to reduce the load carried to zero. This means that the optimizer created a result that duplicated the severed jumper strap.

Table 3 - Optimization Parameters for the 0 degree spreader bar angle case

| Parameter | Units | Estimated | | Optimized Result |
|---------------------------|-----------------|-----------|---------|------------------|
| | | Minimum | Maximum | |
| Halyard Force +Y | lbs | 5.00 | 7.00 | 6.17 |
| Halyard Force -Z | lbs | 5.00 | 7.00 | 7.28 |
| Jumper Strap Slack +Y | inch (+ slack) | 0.00 | 0.92 | -0.057 |
| Jumper Strap Slack -Z | inch (+ slack) | 0.00 | 0.92 | -0.346 |
| Jumper Strap Slack Tack | inch (+ slack) | 0.00 | 1.01 | 0.142 |
| In-plane y-halyard motion | inch (+ inward) | -1.00 | 1.00 | 0.713 |
| Vertical y-halyard motion | inch | -1.00 | 1.00 | 0.851 |
| In-plane z-halyard motion | inch (+ inward) | -1.00 | 1.00 | 0.977 |
| Vertical z-halyard motion | inch | -1.00 | 1.00 | 0.154 |
| Vertical tack motion | inch | -0.50 | 0.50 | 0.746 |

A side-by-side comparison of test and analysis results for the 22.5 degree spreader bar case is shown in Figure 13. When the spreader bars were tilted to 22.5 degrees, one corner of the sail moved up, while the opposing corner moved down. The yellow crosses indicate the points of maximum and minimum deflections relative to a flat sail and 0 degree spreader bars. The maximum error for the 22.5 degree case was only 1.40 inches with an RMS error of 0.77 inches.

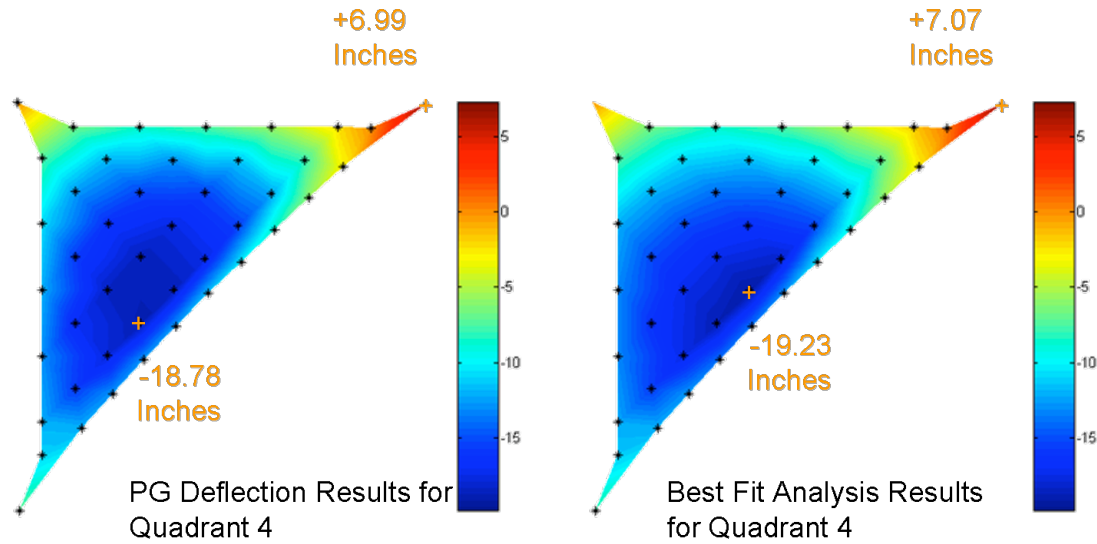


Figure 13 - Billow shape of quadrant 4 at 22.5 degrees for Photogrammetry (PG) and Best Fit Analysis

The optimized parameters for the 22.5 degree spreader bar case are shown in Table 4. While the parameters are not the same as in the 0 degree case, they show similar trends. The jumper straps at the halyards show very low values, which means the jumper strap carries significant load. Although the jumper straps went into tension, this does not necessarily mean an incorrect analysis. Likely the modulus and/or cross-sectional area of the strap were modeled using values lower than the real ones, so the extra contraction is required to obtain the same force. In the 22.5 degree spreader bar case, even though the jumper strap is extended more than in the 0 degree case, it does carry a small amount of load.

Table 4 - Optimization Parameters for the 22.5 degree spreader bar angle case

| Parameter | Units | Estimated | | Optimized Result |
|---------------------------|-----------------|-----------|---------|------------------|
| | | Minimum | Maximum | |
| Halyard Force +Y | lbs | 5.00 | 7.00 | 7.00 |
| Halyard Force -Z | lbs | 5.00 | 7.00 | 7.15 |
| Jumper Strap Slack +Y | inch (+ slack) | 0.00 | 0.92 | 0.035 |
| Jumper Strap Slack -Z | inch (+ slack) | 0.00 | 0.92 | -0.122 |
| Jumper Strap Slack Tack | inch (+ slack) | 0.00 | 1.01 | 0.156 |
| In-plane y-halyard motion | inch (+ inward) | -1.00 | 1.00 | 0.361 |
| Vertical y-halyard motion | inch | -1.00 | 1.00 | 0.517 |
| In-plane z-halyard motion | inch (+ inward) | -1.00 | 1.00 | 0.929 |
| Vertical z-halyard motion | inch | -1.00 | 1.00 | 0.249 |
| Vertical tack motion | inch | -0.50 | 0.50 | 0.589 |

SYSTEM DYNAMICS

Two dynamic FEMs were created and compared to the test data. The main model was the system level model that included the four sails and the four masts. A second model was created to compare only the mast dynamics.

MAST DYNAMICS

For the dynamic analysis of the masts, unlike the system model, the hub structure was included. Without the hub structure, the masts are not connected and would function as four separate structures.

The mast test setup was slightly different than the system setup. Aside from the sails being detached, the gravity compensator mechanism was removed because it produces an unstable torque on the masts without the halyard tension. Without the mass of the gravity compensator, the negator springs supporting the mast tips exerted more force than is necessary to support the boom tip at its neutral position. To alleviate this problem, the cables supported the mast tips instead of the negators.

Three parameters were varied to obtain analytical frequencies that would match the test results. The modulus of the longerons and diagonals was reduced less than 10% and the concentrated masses at the tip were rearranged. The reduction of the longeron and diagonal stiffness served to reduce the bending frequencies. The tip mass was redistributed more towards the center of the mast which reduced the moment of inertia and increased the torsional frequency.

Table 5 - Comparison of test, baseline and tuned mast frequencies

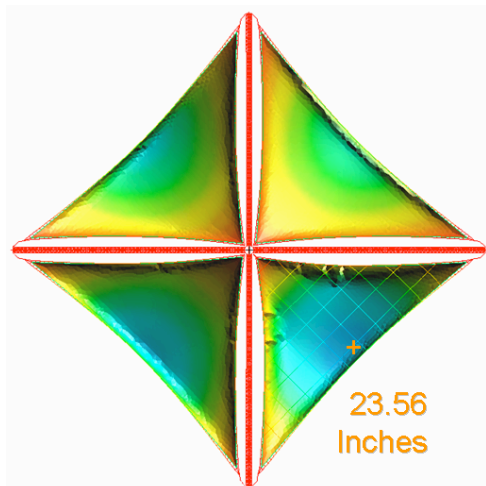
| | Test | | Baseline | | Tuned | |
|---------------|-------|-------|----------|-------|-------|-------|
| | Min | Max | Min | Max | Min | Max |
| Horz. Bending | 0.797 | 0.813 | 0.843 | 0.845 | 8.120 | 8.140 |
| Boom Twist | 2.39 | 2.41 | 2.20 | 2.21 | 2.40 | 2.40 |
| Vert. Bending | 5.14 | 5.30 | | | | |
| Vert. Bending | 7.47 | 7.87 | 8.29 | 8.29 | 7.77 | 7.77 |

Table 5 shows the frequencies from testing and both the baseline (pre-test) and tuned (post-correlation) analyses. None of the analyses showed modes that corresponded to modes in the 5.14-5.30 Hz range that were found during testing. This is most likely the first vertical mast-bending mode that is suppressed in the analysis by the cable suspension. The mode at 7.77 Hz in the tuned analysis looks identical to the second mast-bending mode and aligns very well with the test data.

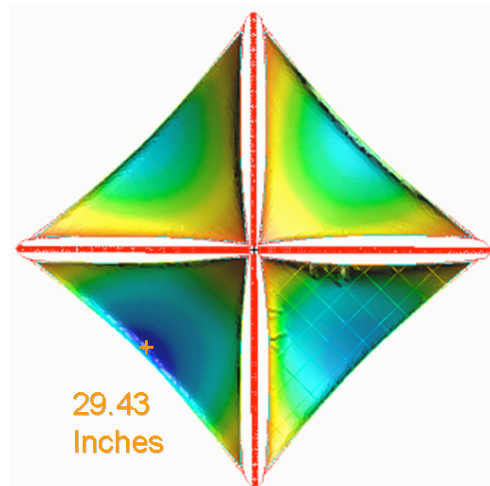
SYSTEM DYNAMICS

The baseline system dynamics model was modified to better match the test setup and to utilize the results from the static shape optimization. The model was analyzed with the tuned masts, the updates to quadrant 4, and the tack line jumper strap was removed (the jumper strap was severed before dynamics testing). The one aspect of the optimized solution that was not used was the halyard load because the configuration changed and the halyard loads were measurably different. Since the dynamics testing was conducted after the sails had been moved a number of times, there was no expectation that the halyard loads during the static testing were the same loads as for dynamic testing.

Initially the model was run with nominal halyard loads set at 6 lbs for all eight halyards. It was discovered after studying the test data that the halyard loads varied considerably from their nominal values. The halyards for quadrant 3 averaged 4.0 lbs. whereas the halyards for quadrant 4 averaged 5.76 lbs. A second model was then run with all eight halyards being assigned the loads found during testing. Figure 14 shows the system with the nominal halyard tension on the left and the deflections with the independent halyard tensions on the right. The large change in deflection also meant significant changes in frequency, especially in boom twist and boom horizontal bending, as seen in Table 6.



Nominal 6 lbs. Halyards



Independent Halyard Tensions

Figure 14 - Effect of using independent halyard tensions to replace the nominal 6 lbs. halyard tensions

After updating the halyard loads and processing the results, it was discovered that the tack line loads still did not match the test data. The halyard loads were adjusted to bring them more in line with the test data. It should be noted that higher confidence was given to the tack line load cell than the load cells used for the halyards.

The modes that were found in the analysis and in the test can be divided into two categories. There are modes that are dominated by the behavior of the masts, and there are modes where the sails dominated the motion. Because the masts outweigh the sails by an order of magnitude, the mast-dominated modes created significant motion in the sails. The motion and shape of the sail in the mast-dominated modes is determined by the amplitude of the motion of the halyard corners and to the mode proximity to the sail mode. Thus for the mast-dominated modes, the frequency is more important than obtaining an exact match in shape.

Table 6 - Effects of independent halyard tensions on model frequencies

| 6 lbs. Halyard Tension | | | | | |
|------------------------------|----------------|----------------|----------|----------------------|----------------------|
| Boom | | | Quadrant | 1 st Sail | 2 nd Sail |
| Twist | Vert. Bend | Horz. Bend | | | |
| 0.51 hz | 0.62 hz | 1.07 hz | 1 | 1.01 hz | 1.54 hz |
| 0.52 hz | 0.64 hz | 1.15 hz | 2 | 0.99 hz | 1.50 hz |
| 0.52 hz | 0.64 hz | 1.16 hz | 3 | 0.96 hz | 1.40 hz |
| 0.53 hz | 0.65 hz | 1.22 hz | 4 | 0.91 hz | 1.46 hz |
| Min | 0.51 hz | 0.62 hz | | 0.91 hz | 1.40 hz |
| Max | 0.53 hz | 0.65 hz | | 1.01 hz | 1.54 hz |
| Independent Halyard Tensions | | | | | |
| Boom | | | Quadrant | 1 st Sail | 2 nd Sail |
| Twist | Vert. Bend | Horz. Bend | | | |
| 0.42 hz | 0.61 hz | 0.94 hz | 1 | 0.95 hz | 1.45 hz |
| 0.42 hz | 0.62 hz | 0.99 hz | 2 | 0.97 hz | 1.55 hz |
| 0.44 hz | 0.62 hz | 1.04 hz | 3 | 0.78 hz | 1.13 hz |
| 0.44 hz | 0.63 hz | 1.11 hz | 4 | 0.90 hz | 1.49 hz |
| Min | 0.42 hz | 0.61 hz | | 0.78 hz | 1.13 hz |
| Max | 0.44 hz | 0.63 hz | | 0.97 hz | 1.55 hz |

The dominant boom modes in the frequency range tested were the boom torsion near 0.5 Hz, the vertical boom bending around 0.65 Hz, and the horizontal boom bending at 1.0 Hz. Figure 15 shows the frequency response functions (FRFs) for all measured targets from one of the tests along with frequency bands representing the range in which the mast-dominated modes were found. In the analysis there are four mast modes of each type from the four masts.

The first band of modes corresponded to the boom twist mode and occurs in the analysis in the range of 0.42-0.44 Hz. These modes were qualitatively similar to measured modes at 0.5 Hz. The second band of modes corresponded to the vertical boom bending modes. These modes occur in the range from 0.61 to 0.63 Hz in the analysis, with tested modes found at 0.625 Hz. The final band of boom dominant modes was the horizontal boom bending modes. There was much more spread in the analysis for these modes because of the discrepancies in the halyard loads. The analysis showed modes from 0.94 to 1.11 Hz whereas testing frequencies occurred from 0.93 to 1.14 Hz.

Examples for each of the three types of boom modes are shown in Figure 16. The mode on the left is a good example of the boom twist mode, the left center mode is a vertical boom-bending mode, and the two modes on the right are different horizontal boom bending modes. Figure 17 shows operational deflection shapes (ODS) obtained during testing that correspond to the boom dominant modes found in the analysis. Due to the time constraint, only quadrant 4 data was available to evaluate the ODS. However, qualitatively the ODS matched those in the analysis.

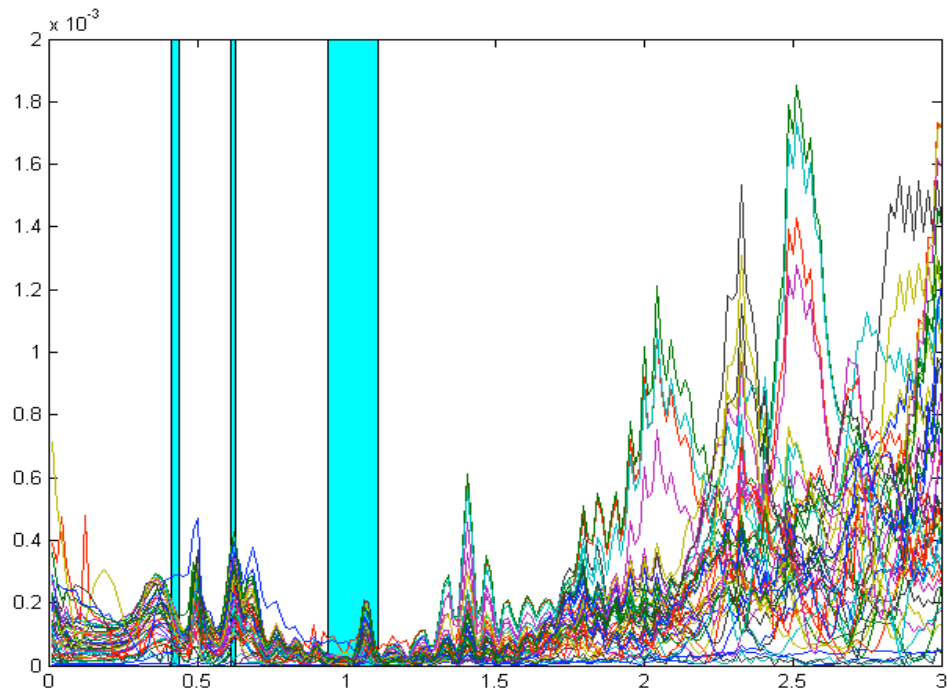


Figure 15 - FRFs from the test results and frequency bands for the analytical mast dominant modes

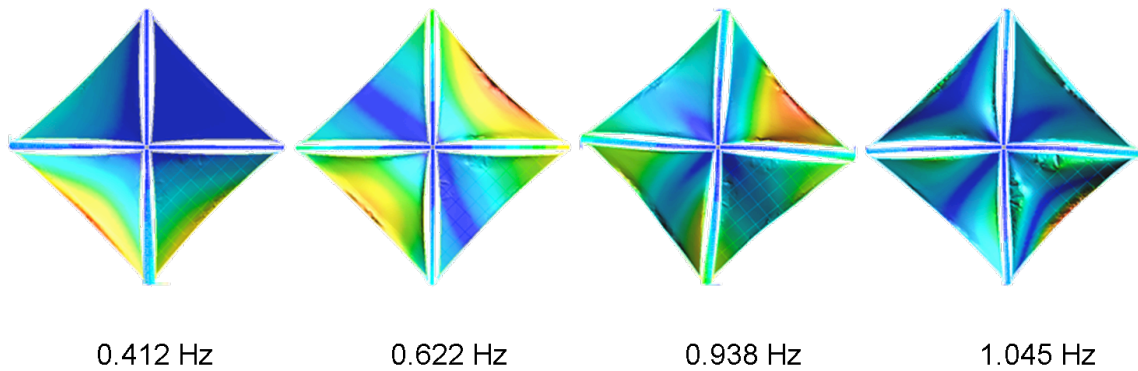


Figure 16 - Examples of boom dominant modes from analysis

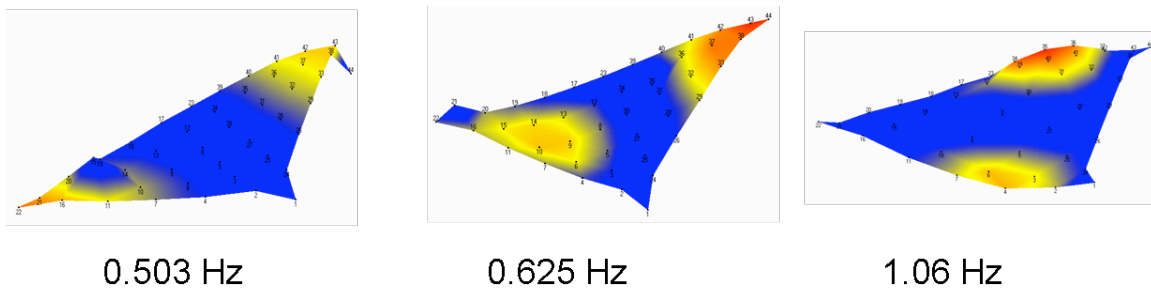


Figure 17 - Examples of boom dominant modes from test results

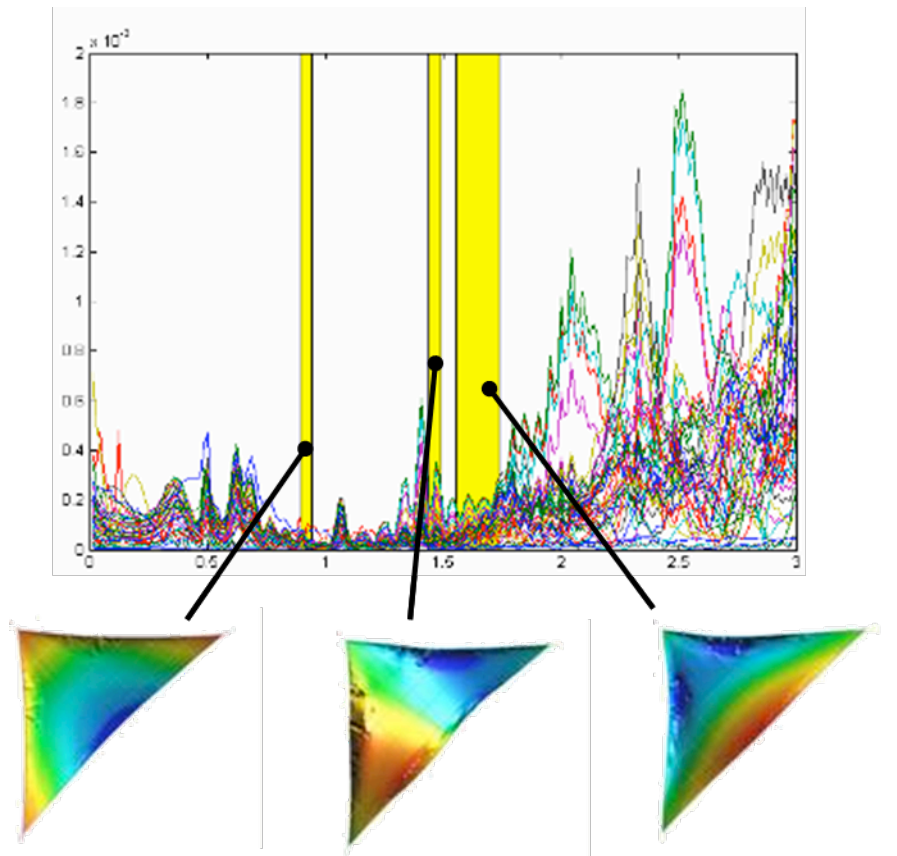


Figure 18 - FRFs from the test results and frequency bands for the analytical sail dominant modes

The sail dominated modes did not correlate as well as the mast-dominated modes. Figure 18 shows FRFs from the test data along with the ODS for the sail dominated modes. Within the frequency bands shown in yellow, quadrant 4 behaves in a manner similar to the images shown below the graph. The first mode was a billow type mode and was exhibited by quadrant 4 in two different system modes. The second mode was a sideways rocking motion about the sail axis of symmetry or see-saw mode which occurred in many of the mast modes. The third mode is an inboard-outboard rocking mode that quadrant 4 exhibited in five different sail dominated system modes and a number of boom dominated system modes (not included in the frequency band). While the frequency bands in some cases was close to peaks in the FRFs, the corresponding ODS at those frequencies do not resemble the analytical modes.

CONCLUDING REMARKS

System level analysis efforts conducted for NASA's solar sails under In Space Propulsion program illustrate the enormous analysis challenges associated with geometrically non-linear effects and numerical convergence of analytical models. A 20 meter solar sail system was modeled using finite element analysis with MSC/NASTRAN. The models were validated with the test results for prediction of the static and dynamic response of the system. Correlation of the static deflections, vibration modes, and frequencies for test and analysis was very difficult with mixed results. However, static deformations of the sail under gravity loads were successfully reconciled to less than 6 % error after parameter adjustments. However, dynamic data correlation showed qualitatively similar behavior but one to one comparisons were questionable. Nonetheless, our objective to study and develop computationally efficient models for ultra-lightweight solar sail structures was met.

ACKNOWLEDGMENTS

The authors would like to thank Mr. Jim Gaspar from Structural Dynamics Branch and Mr. Tom Jones from Advanced Sensing and Optical Measurement Branch, both at NASA Langley Research Center, for conducting the tests of the 20 meter system.

REFERENCES

1. Wright, J., **Space Sailing**, Taylor and Francis Publishers, (1992).
2. McInnes, C. R., **Solar Sailing: Technology, Dynamics, and Mission Applications**, Springer-Praxis Series in Space Science and Technology, (1999).
3. Chmielewski, A.B. **Advanced Concepts," Gossamer Spacecraft: Membrane and Inflatable Structures Technology for Space Applications**, Edited by C.H.M. Jenkins, Progress in Astronautics and Aeronautics, Vol. 191, American Institute of Aeronautics and Astronautics, Reston, VA, (2001).
4. Taleghani, B., Sleight, D. W., Muheim, D.M., Belvin, W. K. and Wong, J. T., **Assessment of Analysis Approaches for Solar Sail Structural Response**, 39th AIAA/ASME/SAE/ASEE Joint Propulsion Conference, Huntsville, AL, AIAA-2003-4796,
5. Taleghani, B., Lively, P., Gaspar, J. Murphy, D. and Trautt, T., **Dynamic And Static Shape Test/Analysis Correlation of a 10-Meter Quadrant Sail**, 46th AIAA/ ASME/ASCE/AHS/ASC Structures, Structural Dynamics, and Materials Conference and Exhibit, Austin, TX, AIAA-2005-2123.
6. Greschik, G. and Mikulas, M.M., **Design Study of a Square Solar Sail Architecture**, 42nd AIAA/ ASME/ASCE/AHS/ASC Structures, Structural Dynamics, and Materials Conference and Exhibit, Seattle, WA, AIAA-2001-1259.
7. Murphy, D., Murphey, T., and Gierow, P., **Scalable Solar-Sail Subsystem Design Concept**, AIAA Journal of Spacecraft and Rockets, Volume 40, No. 4, pp. 539-547, (July-August 2003).
8. Murphy, D., Trautt, T., McEachen, M., Messner, D., Laue, G., and Gierow, P., **Progress and Plans for System Demonstration of a Scalable Square Solar Sail**, AAS 04-105, 14th AAS/AIAA Space Flight Mechanics Meeting, (2004).
9. MSC/NASTRAN **Handbook for Nonlinear Analysis**, S.H. Lee, editor, The MacNeal Schwendler Corporation, 1992.
10. MSC.NASTRAN Quick Reference Guide version 2001, MSC.Software Corporation, 2001.
11. St. Clair, A. K., and Slempe, W. S., SAMPE Journal, Vol. 24, 1985, p.28.
12. Krishnamurthy, T., Romero, V. J., **Construction of Response Surface with Higher Order Continuity and its Application to Reliability Engineering**, 43rd AIAA/ASME/ASCE/AHS/ASC Structures, Structural Dynamics, and Materials Conference, Denver, CO, AIAA-2002-1466